Applied Catalysis B: Environmental 238 (2018) 70–81

Contents lists available at ScienceDirect

Applied Catalysis B: Environmental

journal homepage: www.elsevier.com/locate/apcatb

Persulfate-mediated catalytic and photocatalytic bacterial inactivation by magnetic natural ilmenite

Dehua Xia[a,b,c], Huanjunwa He[a], Huadan Liu[a], Yunchen Wang[a], Qing Zhang[a], Yan Li[d], Anhuai Lu[d], Chun He[a,b,*], Po Keung Wong[c,**]

[a] School of Environmental Science and Engineering, Sun Yat-sen University, Guangzhou, 510275, China
[b] Guangdong Provincial Key Laboratory of Environmental Pollution Control and Remediation Technology, Guangzhou, 510275, China
[c] School of Life Sciences, The Chinese University of Hong Kong, Shatin, NT, Hong Kong, China
[d] The Key Laboratory of Orogenic Belts and Crustal Evolution, School of Earth and Space Sciences, Peking University, Beijing, 100871, China

ARTICLE INFO

Keywords:
Ilmenite
Persulfate
Bacterial inactivation
Photocatalysis
Visible light

ABSTRACT

In this study, a natural occurring ilmenite was successfully developed as an efficient catalyst/photocatalyst for bacterial inactivation coupling with persulfate (PS) under visible light (Vis) irradiation. The excellent bacterial inactivation is demonstrated by the result that the bactericidal efficiency in the ilmenite/PS/Vis process reached 6 $\log_{10}$ cfu/mL within 30 min as compared to that of 1.5 $\log_{10}$ cfu/mL for the ilmenite/Vis process and 4 $\log_{10}$ cfu/mL for the ilmenite/PS under same conditions. Integrated with the electron paramagnetic resonance analysis, electrochemical measurements and photoluminescence spectroscopic analysis, the enhanced performance was attributed to the accelerated capture of photo-generated electrons by PS and ≡Fe(II) of ilmenite promoted PS activation vice versa to collectively generate more radicals for *E. coli* inactivation in the ilmenite/PS/Vis process. For the first time, the generation of singlet oxygen ($^1O_2$) was proved to be the primary bactericidal agent other than $\cdot SO_4^-$ and $\cdot O_2^-$, which caused leakage and mineralization of *E. coli* intracellular components. Impressively, the $^1O_2$-mediated ilmenite/PS/Vis system showed good inactivation performance in authentic water body and maintained good reusability in the pilot-scale 25 L reactor. This work highlights the great potential of natural ilmenite as catalyst and elucidated a new opportunity for persulfate remediation of controlling microbial water contaminants.

1. Introduction

Worldwide, 2 billion people are reliant on a drinking water source contaminated with feces, resulting in over half a million deaths each year related to the consumption of unsanitary water [1]. A suite of chemical disinfection methods like chlorination are considered as the most practical solution to provide safe drinking water, but it requires a consumable material, and presents risks to the promotion of persistent antibiotic resistance and formation of disinfection byproducts [2,3]. In recent decades, utilization of solar energy for pathogenic bacteria killing represents an economic and clean approach like reusable photocatalyst, which can produce *in situ* high oxidative species like ·OH to attack cells [4–6]. Till now, various types of visible-light-driven (VLD) photocatalysts have been developed to photocatalytically inactive bacteria, involving modified TiO_2 and non-TiO_2 based materials, such as metal oxides, sulfides, and non-metal g-C_3N_4 and red phosphorous, etc. [7–9]. However, most photocatalysts are often synthesized from expensive chemicals in high purity and may involve complex steps under special conditions. Hence, the cost of these synthesized photocatalysts in a large quantity can be very high.

Recently, naturally occurring minerals such as sphalerite, pyrrhotite were found to behave like semiconductors, exhibiting bactericidal activity under VL irradiation [10–12]. The VL-driven (VLD) photocatalytic activities of these natural minerals were mainly attributed to the substitution of transition metal like Fe, Cu and surface defects [13,14]. The doped transition metal can narrow the band-gap, and the surface defect can capture the photo-generated electrons to collectively work for the generation of radicals [15,16]. In contrast with the synthetic catalysts, these natural minerals can be readily supplied in large quantities at low cost. Moreover, the specific ferromagnetic properties of these minerals, mainly due to Fe-containing can facilitate its separation and recycling after utilization [11,12].

* Corresponding author at: School of Environmental Science and Engineering, Sun Yat-sen University, Guangzhou, 510275, China.
** Corresponding author at: School of Life Sciences. The Chinese University of Hong Kong, Shatin, NT, Hong Kong, China.
E-mail addresses: hechun@mail.sysu.edu.cn (C. He), pkwong@cuhk.edu.hk (P.K. Wong).

https://doi.org/10.1016/j.apcatb.2018.07.003
Received 18 April 2018; Received in revised form 26 June 2018; Accepted 1 July 2018
Available online 03 July 2018
0926-3373/

Unfortunately, the fast recombination of photo-generated electrons and holes leads to unsatisfactory photocatalytic efficiencies of the reported natural minerals, which limits its application [17]. Thermal modification has been reported to enhance their photocatalytic performance through intensifying its inner electron-hole separation [4,12,14]. For instance, the calcined natural pyrrhotite had 3-times *E. coli* inactivation rate than that of pristine pyrrhotite, attributed to the formation of Z-scheme electron transfer system [12]; while calcined sphalerite achieved 5-fold bactericidal efficiency than raw sphalerite due to the occurrence of $ZnO/ZnFe_2O_4$ structure [14]. But the inevitable disadvantages of calcination like toxic gas (e.g. H_2S) release and relative high cost may still restrict its application. Alternatively, another important and feasible strategy to reduce charge carrier recombination probability is the addition of oxidants such as hydrogen peroxide (H_2O_2), persulfate (PS) and peroxymonosulfate (PMS) through the immediate trapping of photogenerated electrons [18–21]. For instance, Gao et al. found that the introduced PS can be activated by photo-generated electrons of excited kaolinite-supported iron oxide to generate $\cdot SO_4^-$ and more $\cdot OH$, resulting in the accelerated photocatalytic degradation of AO7 [22]. Actually, $\cdot SO_4^-$ based advanced oxidation process (AOP) may hold promise to be more effective than conventional water disinfection processes in inactivating biohazards due to their more powerful oxidation capabilities and lower tendency to form DBPs [23–25]. Moreover, natural minerals enriched in transition metals like Fe(II) are also beneficial to catalyze PS into $\cdot SO_4^-$ [26,27]. Inspired by these excellent attempts of introducing electron acceptors to the mineral based-photocatalytic system, more natural minerals are exploited and applied as a photocatalyst/catalyst to inactivate bacteria in the presence of PS.

There are still many controversies in the generated radicals by PS mediated reaction. At present, most PS activation focused on the generation of $\cdot SO_4^-$ as primary ROS. For instance, Gao et al. suggested photogenerated electron can reduce PS to generate $\cdot SO_4^-$ and $\cdot OH$ for RhB degradation in MIL-53(Fe)/PS/Vis system [28]. Nevertheless, the activation of PMS via Ag/g-C_3N_4 has been demonstrated by Wang et al., in which the oxidation of RhB was contributed principally by the BMPOX, a complex with $\cdot SO_4^-$ [29]. Despite the continuous research interest in the generation of $\cdot SO_4^-$, studies on $^1O_2$ formation involved in PS reaction are sparse [30]. Generally, $^1O_2$ can be produced through a photochemical process using the photo-induced energy transfer to molecular oxygen (photosensitization) [31,32]. In recent, $^1O_2$ was found to be transformed by $\cdot O_2^-$ through a non-photo-induced method in the CNT/PS system. Singlet oxygen ($^1O_2$) is a nonradical ROS, which has been largely used for the oxidation of organic matter due to its electrophilic nature, which may be beneficial for *E. coli* inactivation [33]. Therefore, the detailed mechanism for the ROS generation via PS mediated process need to be clarified.

As a titanate of ferrous iron mineral, ilmenite ($FeTiO_3$) is an antiferromagnetic semiconductor with a band gap varying at 2.4–2.9 eV, with good potential applications in photocatalytic and catalytic reactions [34,35]. Herein we report the photocatalytic/catalytic inactivation of *Escherichia coli* over ilmenite under visible light (VL) irradiation. Light emitting diodes (LEDs) lamp was applied in this work due to its energy saving, narrow band emission and long life-span [36,37]. To accelerate the inactivation of *E. coli* over ilmenite, sodium persulfate (PS, $Na_2S_2O_8$) was added into the reaction. Meanwhile, its efficiency in terms of radical type and yield, as well as *in situ* ATR-FTIR (attenuated total reflectance-Fourier transform infrared) spectroscopic and photoelectrochemical characterization, were collectively applied to analyze the PS activation process occurring on the ilmenite surface, including both catalytic and photocatalytic mechanisms. Then the primary oxidizing species produced in the system were identified by chemical quenching and trapping methods with crucial parameters discussed. Moreover, to test the activity and applicability of ilmenite/PS/Vis system, the inactivation kinetics of *E. coli* were measured in a pilot-scale reactor (25 L) at varying ilmenite/PS doses and authentic wastewater matrix. This work provides a cost-effective method for biohazards inactivation.

2. Materials and methods

2.1. Chemicals

Phenol, methanol, and *tert*-butyl alcohol (TBA) were obtained from Sigma-Aldrich, USA. Sodium persulfate (PS), catalase, 5,5-dimethyl-1-pyrrolidine N-oxide (DMPO), 2,2,6,6-Tetramethyl-4-piperidinol (TMP, 99%) were purchased from Aladdin, China. The pristine ilmenite ($FeTiO_3$) mineral was collected from a mining site in China, which was previously machine-crushed, and then selected by an electromagnetic and gravity separator. Before use, the picked ilmenite was sieved at 300-mesh to obtain powders with size smaller than 38 μm.

2.2. E. Coli disinfection process

(i) Laboratory mode: The *E. coli* culture was incubated in Nutrient Broth (NB, Tissue culture grade, Amresco) at 37 °C for 12 h. Then the *E. coli* suspension was obtained after centrifuging the above culture at 15,000 rpm for 1 min. The ilmenite of 0.2 mg/mL was added to analyze its disinfection performance on *E. coli*. 1 mL of the reaction suspension was sampled every 5 min interval and immediately transferred into the biosafety cabinet for spreading on the Nutrient Agar plate of petri dish. After incubation at 37 °C for 24 h, the colony forming units of *E. coli* were counted to determine the survival ratio.

(ii) Pilot-scale mode: A pilot-scale treatment device (25 L, cylindrical stirred-tank-reactor) was designed and fabrication for wastewater treatment. Appropriate concentrations (to final cell density of 10^5 cfu/mL) of bacterial cells were added into the reaction mixture. All experiments for treatments and controls were conducted in triplicates. The white LED lamp belt surrounding the reactor and stirrer were turned on to provide VL and mixing, respectively. During the inactivation process, treated sample was collected through the respective a paired inlet and outlet.

2.3. Reactive species and persulfate analyses

(i) Electron paramagnetic resonance (EPR) analysis: A solution containing 10 mM DMPO or TMP and 0.5 mM PS, and then 50 mg ilmenite was added to initiate the reaction. After 0, 5, 10 min of reaction, samples were taken and analyzed on a JEOL FA200 EPR spectrometer; (ii) Concentration of persulfate: At each time interval, 1 mL sample was transferred to a 10 mL glass vial containing 9 mL DI water, followed by adding 0.05 g $NaHCO_3$ and 1 g KI powder [26]. The mixture was then hand shaken and set for equilibrium for 15 min before measuring the absorbance at 400 nm on a UV–vis spectrophotometer (Lambda 25, Perkin Elmer Inc., USA).

2.4. Cell destruction process

(i) Cell viability assay: *E. coli* cells treated at various times were collected and tested using a LIVE/DEAD®-BacLight Bacterial Viability Kit (Molecular Probes, USA) with a fluorescence microscope; (ii) Leakage of intracellular substance: 1 mL of *E. coli* suspension was added into ilmenite/PS solution. After the reaction, sodium thiosulfate (0.1 mol/L) was added into above solution to mix for 3 min, then centrifuged at 10,000 rpm for 15 min. After that, total nitrogen (TN) concentration in the supernatant was measured using spectrophotometric method [38]. To clarify the composition, extracellular DNA and protein were determined as well [39]; and (iii) ATP measurement: Total ATP concentration was measured using BacTiter-Glo reagent (G8231, Promega, America) [38]. Samples were preheated at 38 °C for 10 min, and reagents were preheated at 38 °C for 2 min, then 500 μL samples and 50 μL reagents were mixed for 20 s to measure its luminescence

intensity. Extracellular ATP was quantified after the filtration of a sample with 0.1 μm filter using a sterile 10-mL syringe, while intracellular ATP was calculated by subtracting extracellular ATP from total ATP [40].

2.5. Effect of water matrix

Two authentic water samples were collected, including secondary sewage treatment effluent of Shatin wastewater treatment plant, and Weiyuan Lake of The Chinese University of Hong Kong. The water quality parameters such as turbidity, suspended solid (SS), total phosphate (TP), total nitrogen (TN), and ammonia, have been analyzed before treatment. Before test, disinfection of bacteria cells in the water samples by ilmenite was conducted. Culture of the selected bacteria (*E. coli*) was used spiked to the water samples to 5 $1og_{10}$ cfu/mL concentrations for the feasibility study.

3. Results and discussion

3.1. Materials characterization

As shown in Fig. 1a, the 2-Theta peaks at 23.9°, 32.65°, 35.3°, 40°, 48°, 53°, 61°, 63° in the XRD spectrum of pristine ilmenite indicates the main existence of $FeTiO_3$ phase, in agreement with the JCPDS card no. 21-1276 [41]. SEM image in Fig. 1b indicates ilmenite powders are in a heterogeneous size ranged from 10 to 30 μm and many mechanically ground fractures are observed on its surface. The magnetic loop in Fig. 1c indicates pristine ilmenite possesses an antiferromagnetic property with maximum magnetization of 0.5 emu/g. As shown in Fig. S1, the ilmenite powders can be immediately drawn to one side of the beaker when an external magnet was placed nearby, indicating its great potential for easy recycle. UV–vis DRS spectra in Fig. 1d indicates ilmenite can adsorb light ranged from 200 nm to 500 nm (visible light region). The band gap energy of ilmenite mineral was estimated from a plot of $(h\nu)^2$ as a function of the photo energy ($h\nu$) to be 2.62 eV, close to the previously reported value for $FeTiO_3$ (2.72 eV) [21]. Moreover, the specific surface area of raw ilmenite is about 1.2466 $m^2\,g^{-1}$ without obvious pore structure (Fig. S2).

To explore the elemental composition and the surface electronic states of ilmenite, XPS spectroscopy was further performed. As shown in Fig. 2a, the XPS survey spectrum verified that ilmenite was composed of O, Ti and Fe elements, in which the Fe and Ti contents (weight percentage) in raw ilmenite were 36 and 37%. The nonstoichiometric Fe to Ti ratio revealed vacancies were at the Fe sites in the crystal structure. For the high resolution XPS spectrum of Fe2p (Fig. 2b), the two peaks around binding energy of 711.5 and 725.4 eV were ascribed to Fe 2p 3/2 and Fe 2p 1/2, respectively, and were characteristic of Fe(II) and Fe(III) in $FeTiO_3$ [35]. The calculated ratio of Fe(II)/Fe(III) was 43.76/56.23 for natural ilmenite. Fig. 2c showed the high-resolution Ti 2p spectral region of the ilmenite. The binding energy of the Ti 2p 1/2 and Ti 2p 3/2 core levels at 458.9 eV and 464.8 eV, respectively, together with their separation of 5.7 eV confirmed the valence state of Ti as Ti (IV) in $FeTiO_3$ phase. In the high resolution XPS spectrum of O 1s (Fig. 2d), the appearance of two peaks at 531.5 and 530.2 eV could be respectively attributed to the oxygen components on the Ti-O and Fe-O bonds of $FeTiO_3$ [19,42]. Together with the above characterization results, it can be inferred that the obtained ilmenite is mainly composed of $FeTiO_3$. Apart from Fe and Ti, other Si, Al, K, Ca, Mg, Zn are also existed, based on the EMPA results in Table S1.

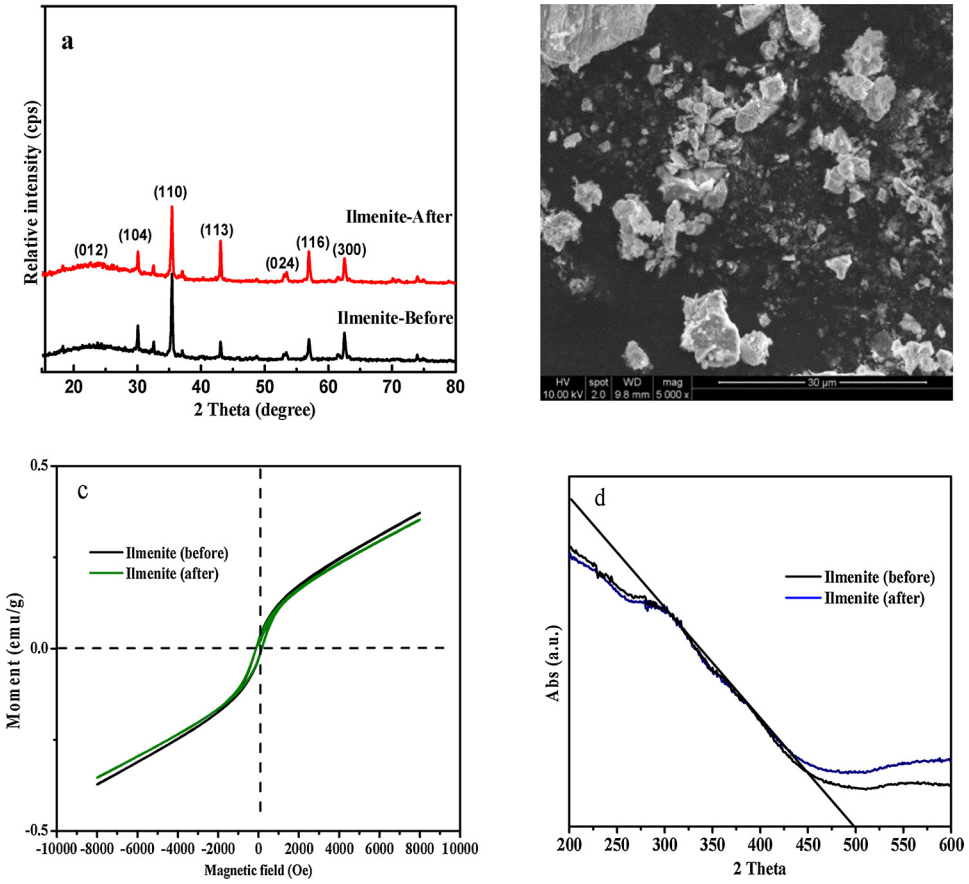

Fig. 1. (a) XRD, (b) SEM, (c) UV–vis spectra and (d) Magnetic loops of pristine and recycled ilmenite.

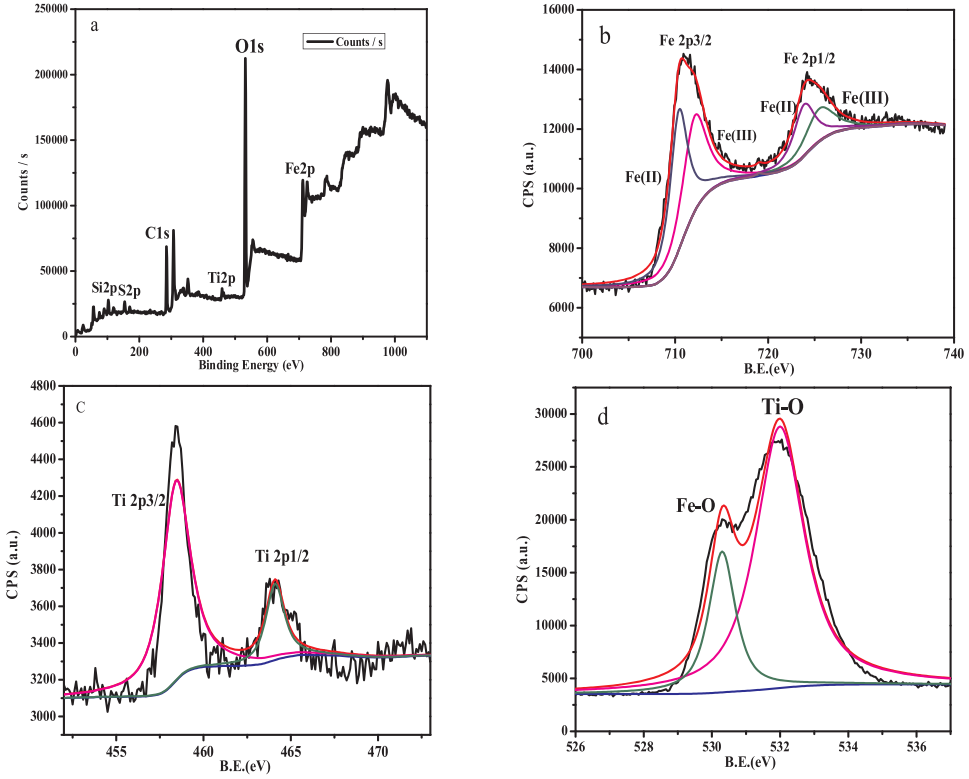

Fig. 2. XPS spectra of ilmenite: (a) the survey spectrum; (b) high-resolution Fe 2p; (c) high-resolution Ti 1s; (d) high-resolution O 1s.

3.2. *E. coli* inactivation in batch-mode

Fig. 3a represents the variation of *E. coli* inactivation as a function of reaction time in various catalytic processes. *E. coli* was quite stable towards incident light because no significant inactivation of *E. coli* was noted after VL irradiation for 30 min. Meanwhile, the ilmenite alone had no obvious adsorption toward *E. coli* with only 0.2 log of cells' loss occurred within 30 min. With PS involved, the negligible loss of *E. coli* in the PS/dark or PS/Vis process revealed that PS alone could neither directly inactivate *E. coli* nor be activated by VL (about 0.3 $\log_{10}$ cfu/mL

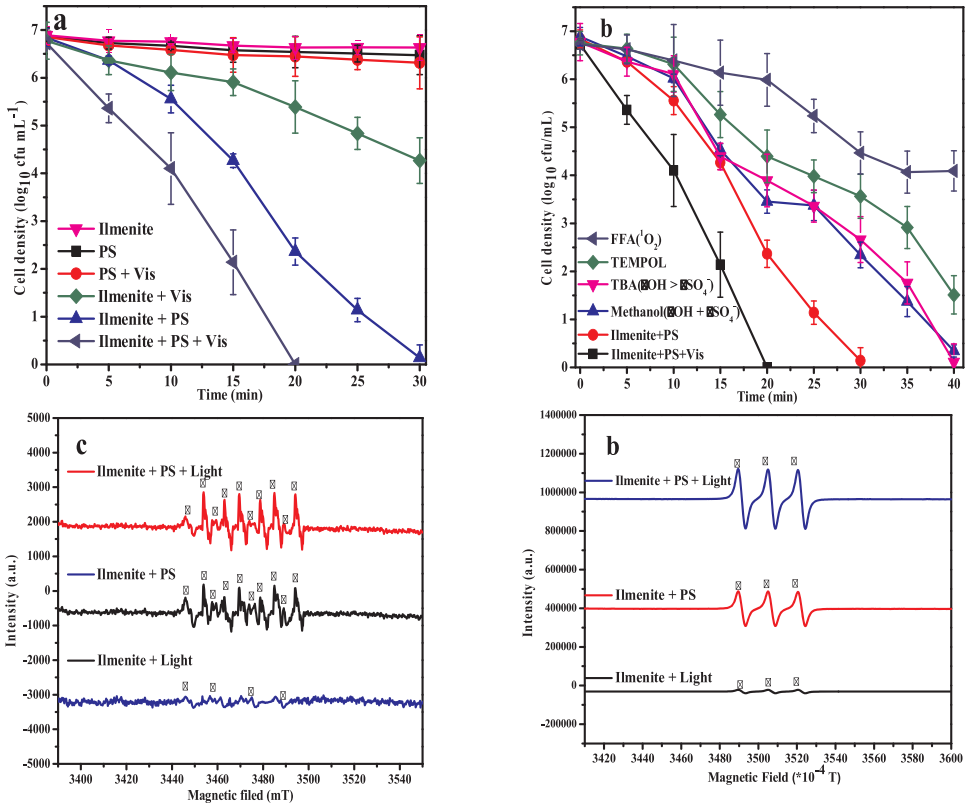

Fig. 3. (a) Bacterial inactivation in 50 mL solution by ilmenite/PS/Vis. (b) Scavenger quenching on bacterial inactivation by ilmenite/PS/Vis system; ESR spectra of DMPO spin-trapping adducts (c) DMPO-$^1O_2$ and DMPO-·$SO_4^{\cdot-}$, (d) DMPO-$^1O_2$ of ilmenite/PS/Vis system. Experimental conditions: [*E. coli*] = 5 $\log_{10}$ cfu/mL, [ilmenite] = 1 g/L, [PS] = 0.5 mM, White LED lamp = 3 mW/cm^2 (VL intensity).

of cell loss). While in the presence of VL illumination, ilmenite showed moderate photocatalytic activity without PS, and about 2.5-log of *E. coli* was inactivated. This could be attributed to the generation of reactive species from the VL illuminated ilmenite, but the photocatalytic performance was limited. Intriguingly, the introduction of PS could significantly enhance the photocatalytic performance of ilmenite, and *E. coli* was nearly completely inactivated within 20 min in the ilmenite/PS/Vis process. Considering that Fe-based ilmenite might activate PS in the catalytic process, the control experiment was further performed in the presence of both PS and ilmenite in the dark, where a 7 $\log_{10}$ cfu/mL cell reduction was observed within 30 min, evidencing the efficient PS activation by ilmenite. Above results suggested that radicals were generated both by persulfate activation and photocatalytic process to collectively responsible for the *E. coli* inactivation.

3.3. Identification of oxidizing species

Generally, ·OH or $\cdot SO_4^-$ are considered to be the primary ROS in the oxidation processes involving PS [43,44]. Therefore, the effects of radical scavengers including methanol, *tert*-butyl alcohol (TBA) were used to investigate the role of ·OH, $\cdot SO_4^-$ in this study. Methanol showed high reactivity with both species ($k_{\cdot OH} = 9.7 \times 10^8\ M^{-1}\ s^{-1}$, $k_{\cdot SO_4^-} = 1.6 \times 10^7\ M^{-1}\ s^{-1}$), while TBA exhibited 1000-times higher reactivity towards ·OH ($k_{\cdot OH} = (3.8–7.6) \times 10^8\ M^{-1}\ s^{-1}$) than $\cdot SO_4^-$ ($k_{\cdot SO_4^-} = (4.0–9.1) \times 10^5\ M^{-1}\ s^{-1}$) [45]. As shown in Fig. 3b, there is no obvious influence in the presence of TBA compared to the methanol addition, suggesting ·OH plays a limited role in the reaction. In contrast, the inactivation of *E. coli* was greatly inhibited in the presence of methanol, suggesting the $\cdot SO_4^-$ is likely generated in the reactions. Especially, recent work indicate PS activation can generate $\cdot O_2^-$ and transform into $^1O_2$ to oxidize 2,4-dichlorophenol (2,4-DCP) besides ·OH, $\cdot SO_4^-$ [46]. Therefore, the role of $\cdot O_2^-$ and $^1O_2$ were also analyzed by adding TEMPOL ($\cdot O_2^-$, $k = 1.2 \times 10^8\ M^{-1}\ s^{-1}$) and furfuryl alcohol ($^1O_2$, FFA, $k = 1.2 \times 10^8\ M^{-1}\ s^{-1}$) as specific scavenger [47]. As shown in Fig. 3b, the inactivation of *E. coli* was significantly inhibited by FFA, indicating $^1O_2$ was the major ROS in the reaction. Meanwhile, as the precursor of $^1O_2$, $\cdot O_2^-$ also played an important bactericidal role, as great inhibition of *E. coli* inactivation was observed by adding TEMPOL (Fig. 3a). As identified above, $^1O_2 > \cdot O_2^- > \cdot SO_4^-$ were major reactive species and responsible for the inactivation of *E. coli* in the ilmenite/PS/Vis system.

Moreover, EPR tests with DMPO/TMP as radical spin trapping agent for various catalytic processes were performed to support the above speculation. As shown in Fig. 3c, the appearance of weak signals (1:1:1:1) observed in the ilmenite/Vis process indicated that ilmenite was limited to generate $\cdot O_2^-$ radicals under VL irradiation, being supportive of the unsatisfactory *E. coli* inactivation in the irradiated ilmenite suspension. Additionally, the results revealed the formation of DMPO-SO_4 and DMPO-O_2 signals in the ilmenite/PS/dark system, indicating that the $\cdot SO_4^-$ and $\cdot O_2^-$ coexisted. The results indicate ilmenite was easy to activate PS without irradiation, attributed to the transition metals like Fe. The sorbed or lattice Fe(II) of ilmenite provides electrons can activate PS to yield surface-adsorbed $\cdot SO_4^-$ radicals and further transform into $\cdot O_2^-$ [48]. Like ZVI or magnetite, the Fe(II) of ilmenite also can supply electrons to O_2 and form $\cdot O_2^-$ vise verse [49]. When VL irradiation was involved, signals of DMPO-$\cdot SO_4^-$ were further enhanced but DMPO-$\cdot O_2^-$ adducts were decreased in the ilmenite/PS/Vis process. The results may suggest that $\cdot O_2^-$ would participate in the reaction to generate $\cdot SO_4^-$. Previous studies have reported that the reaction of $\cdot O_2^-$ with $S_2O_8^{2-}$ could trigger the generation of $\cdot SO_4^-$ [48]. Therefore, it is reasonable to propose that the photo-generated $\cdot O_2^-$ by irradiated ilmenite would participate in the $\cdot SO_4^-$ formation.

Furthermore, as shown in Fig. 3d, a typical three-line EPR spectrum on behalf of $^1O_2$ was also detected in the ilmenite/PS/dark system but limited detection in the ilmenite/Vis system. In general, the $^1O_2$ is mainly produced by a photochemical process using the photoinduced energy transfer to molecular oxygen under sunlight or VL irradiation [50,51]. The present result suggests that the $^1O_2$ formation may use a non-photo induced method between PS and ilmenite, as the generated $\cdot O_2^-$ can then recombine to form into $^1O_2$ [30]. Interestingly, the continuous generation of $^1O_2$ was observed to ascend in the ternary system with VL involved, further indicating that $^1O_2$ is the dominating reactive species involved in the *E. coli* inactivation. Therefore, this suggests the formation of $^1O_2$ involve both functions of photoinduced and non-photoinduced pathway in the ilmenite/PS/Vis system. In addition, $^1O_2$ possess a high selectivity towards electron-rich compounds such as phenols, which can suffer less interference from common background organic and inorganic substances in water [33]. Thus the present $^1O_2$-mediated oxidative system may be beneficial for organic *E. coli* debris mineralization. Above results suggested that the radicals produced from persulfate activation coupled with the photo-generated radicals were responsible for the *E. coli* inactivation, including the great generated $^1O_2$, $\cdot O_2^-$, $\cdot SO_4^-$ in the ilmenite/PS/Vis process.

3.4. Catalytic and photocatalytic mechanism of ilmenite

To analyze the catalytic mechanism occurred on ilmenite surface in the presence of PS or PS + light, the *in-situ* attenuated total reflectance Fourier transform infrared spectroscopy (ATR-FTIR) characterizations were conducted and results were shown in Fig. 4a. Obviously, the adsorptive interaction between PS and ilmenite was evidenced by the enhanced FTIR signals of raw ilmenite (1274 cm^{-1} of the symmetric and 1045 cm^{-1} of asymmetric vibrations of S=O=S of sulfonate group) [52]. Intriguingly, a small band at 1162 cm^{-1} belongs to raw ilmenite was blue-shifted to 1157 cm^{-1} after PS involved, indicating the formation of a complex at ilmenite surface. Previous reports mentioned the oxidation of the surface or lattice Fe(II) of pyrrhotite was fast after adding PS, which can form into ≡Fe(II)/O_3SO=OSO_3 complex to induce the chain reaction of ROS generation [26]. Similarly, it can be inferred that ≡Fe(II) containing ilmenite also can form weak bond of ≡Fe(II)/O_3SO=OSO_3 complex (Eq (1)), which could trigger the broken of O=O bond and subsequently generate ≡Fe(III) and $\cdot SO_4^-$ (Eq. (2)) [53,54]. Meanwhile, the surface H_2O bond of ilmenite at 3100 cm^{-1} became relatively weak after PS involved, suggesting the complex also can promote H_2O molecular into $\cdot O_2^-$ through Eq. (3) [55]. The *in situ* generated $\cdot O_2^-$ can then recombine to form $^1O_2$. Previous studies proposed that the formation of $^1O_2$ involves the recombination of $\cdot O_2^-$, which are produced as an intermediate product in the presence of dissolved oxygen (Eq. (4)) [56]. In addition, after VL involved, the small band occurred at 1162 cm^{-1} of raw ilmenite was more blue-shifted to 1189 cm^{-1} than PS/ilmenite system, suggesting more intensified interaction occurred in the Fe(II)/O_3SO=OSO_3 complex. This is because more electrons of irradiated ilmenite (photoelectron) are involved for PS activation, which are beneficial to generate more reactive species.

$$\equiv Fe(II) + O_3SO = OSO_3^- \rightarrow \equiv Fe(II)\ldots O_3SO = OSO_3^- \quad (1)$$

$$\equiv Fe(II)\ldots O_3SO = OSO_3^- \rightarrow \equiv Fe(III) + \cdot SO_4^- + SO_4^{2-} \quad (2)$$

$$\equiv Fe(II)\ldots O_3SO = OSO_3^- + 2H_2O \rightarrow \equiv Fe(III) + 2SO_4^{2-} + \cdot O_2^- + 4H^+ \quad (3)$$

$$2\cdot O_2^- + 2H_2O \rightarrow {}^1O_2 + H_2O_2 + 2OH^- \quad (4)$$

Moreover, to further explore the enhanced photocatalytic mechanism of ilmenite/PS/Vis process, the band structure of ilmenite with respect to the redox ability of photoinduced charge carriers was also evaluated (Eq. (5)). A typical Mott-Schottky plot of ilmenite measured in the dark is shown in Fig. 4b and the positive slope of the plot revealed a *n*-type semiconductor feature for the prepared ilmenite electrode. The flat-band potential extrapolated for ilmenite was -0.45 V versus SCE, corresponding to -0.21 V versus normal hydrogen electrode

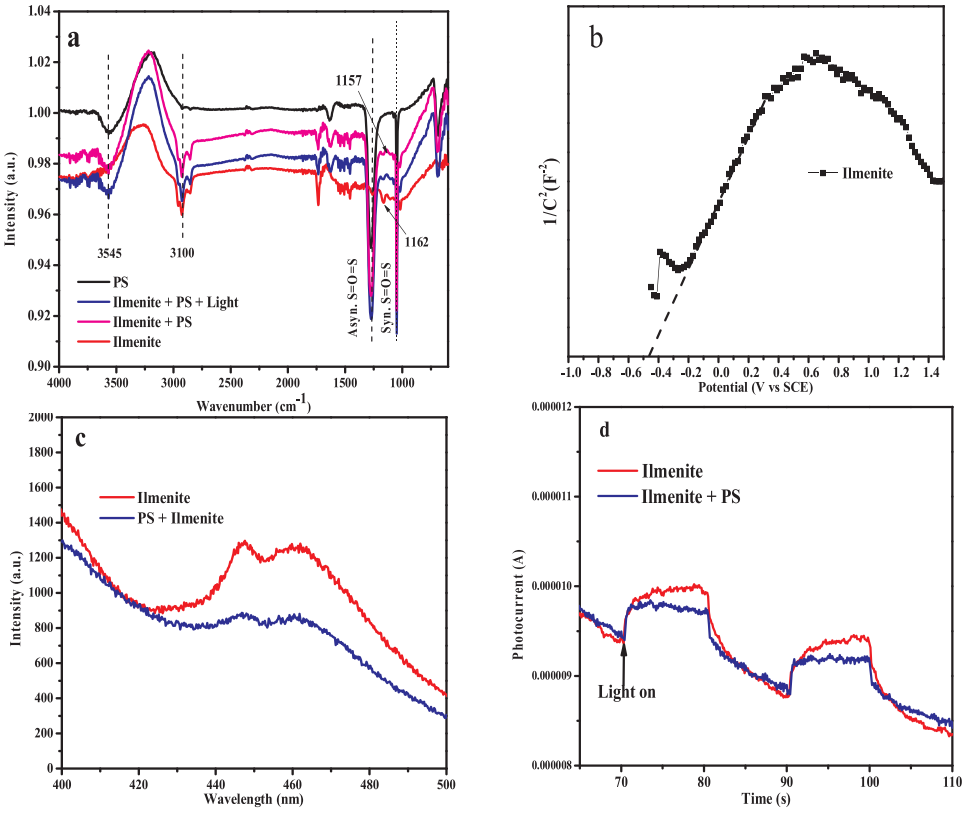

Fig. 4. (a) ATR-FTIR spectra of the PS solution, the ilmenite in water, and the ilmenite in PS solution; (b) Mott-Schottky plots of ilmenite measured at a frequency of 100 Hz in the dark; (c) Photoluminescence spectra for ilmenite suspension with and without the addition of PS; (d) Transient photocurrent responses of ilmenite with and without the addition of PS measured at the potential of 0.2 V versus SCE under VL irradiation. Experimental conditions: [*E. coli*] = 5 $\log_{10}$ cfu/mL, [ilmenite] = 1 g/L, [PS] = 0.5 mM, [Na_2SO_4] = 0.5 M.

(NHE). For *n*-type semiconductors, the flat-band potential was 0-0.1 V higher than the conduction-band potential [57]. This means that the conduction-band minimum (CBM) of ilmenite was negatively shifted to be -0.31 V versus NHE, which was more negative than the redox potential of $\cdot SO_4^-/S_2O_8^{2-}$ [22,28], satisfying the thermodynamic requirements for the production of $\cdot SO_4^-$ via the activation of PS by photogenerated electrons under visible light irradiation (Eq. (6)). Meanwhile, the photogenerated electron by irradiated ilmenite was able to reduce dissolved oxygen into $\cdot O_2^-$ ($O_2/\cdot O_2^-$ = -0.22 eV) (Eq. (7)) [58]. Previous studies have been reported that the reaction of $\cdot O_2^-$ with $S_2O_8^-$ to generate $\cdot SO_4^-$ proceeds according to (Eq. (8)) [56]. Additionally, combination of the band gap energy derived from UV–vis DRS spectra, the VB potential of ilmenite was calculated to be 2.31 V versus NHE, being negative than the redox potential of $\cdot OH/OH^-$ (2.38 V versus NHE) and thus indicating that the hole of ilmenite was not able to oxidize OH^- to ·OH radicals [59]. However, the h^+ still can react with oxygen or $\cdot O_2^-$ to participate in the reaction that generate $^1O_2$ (Eq. (9)) [60].

$$\text{Ilmenite} + h\nu \rightarrow e_{CB}^- + h_{VB}^+ \quad (5)$$

$$S_2O_8^{2-} + e_{CB}^- \rightarrow \cdot SO_4^- + OH^- \quad (6)$$

$$O_2 + e_{CB}^- \rightarrow \cdot O_2^- \quad (7)$$

$$S_2O_8^{2-} + \cdot O_2^- \rightarrow SO_4^{2-} + \cdot SO_4^- + O_2 \quad (8)$$

$$O_2/\cdot O_2^- + h_{VB}^+ \rightarrow {}^1O_2 \quad (9)$$

Furthermore, to identify the accelerated electron transfer in the ilmenite/PS/Vis process, the photoluminescence (PL) and photocurrent tests were employed to explore the efficiency of the charge carrier separation, migration and transfer [57]. The PL spectra for the ilmenite suspension with and without PS addition are shown in Fig. 4c. Upon photoexcitation at 340 nm, the irradiated ilmenite exhibited a broad band at 400–500 nm with a peak at 465 nm. The energy of the PL peak (2.67 eV) basically agreed with the calculated optical band gap energy (2.62 eV) in Fig. 1d. As a further demonstration, the PL intensity for irradiated ilmenite in the presence of PS was lower than that without PS, indicating PS can efficiently inhibit the recombination of photogenerated carriers [61]. This can be interpreted by the fact that the introduced PS, serving as the electron capturer to efficiently capture photogenerated electron, thereby accelerating the *E. coli* inactivation. Similarly, the transient photocurrent responses of ilmenite with and without PS in aqueous Na_2SO_4 solution were also measured under VL illumination with on-off cycles. As shown in Fig. 4d, the introduced PS significantly reduced the photocurrent density of the ilmenite/PS/Vis process in contrast with that of the ilmenite/Vis process. This can be attributed to the capability of PS in efficiently trapping the photogenerated electrons, consistent well with the PL results [22,28]. As identified above, VL irradiated ilmenite exhibited both catalytic and photocatalytic activity, which synergistically trigger the generation of reactive species for enhanced *E. coli* inactivation.

3.5. Role of ROS in mediating cell lesions

The time-dependent nature of the cell-membrane damage, as shown in Fig. 5a, suggested that the lesions on the cells exposed to ilmenite/PS/Vis system are caused by ROS oxidation. Indeed, the results from ROS scavenging test confirm the involvement of ROS ($^1O_2$, $\cdot O_2^-$ and $\cdot SO_4^-$) in the bactericidal action; it is known that $\cdot O_2^-$ are precursors to the more reactive $^1O_2$ species [31]. The oxidation reaction is probably a self-propagating one because sustained exposure of the cells to ROS caused the indentations on the cells to develop into holes that are localized in the midpoint of injured cells (Fig. 5a). It is hypothesized that such damage is likely mediated by ROS whose presence could initiate a

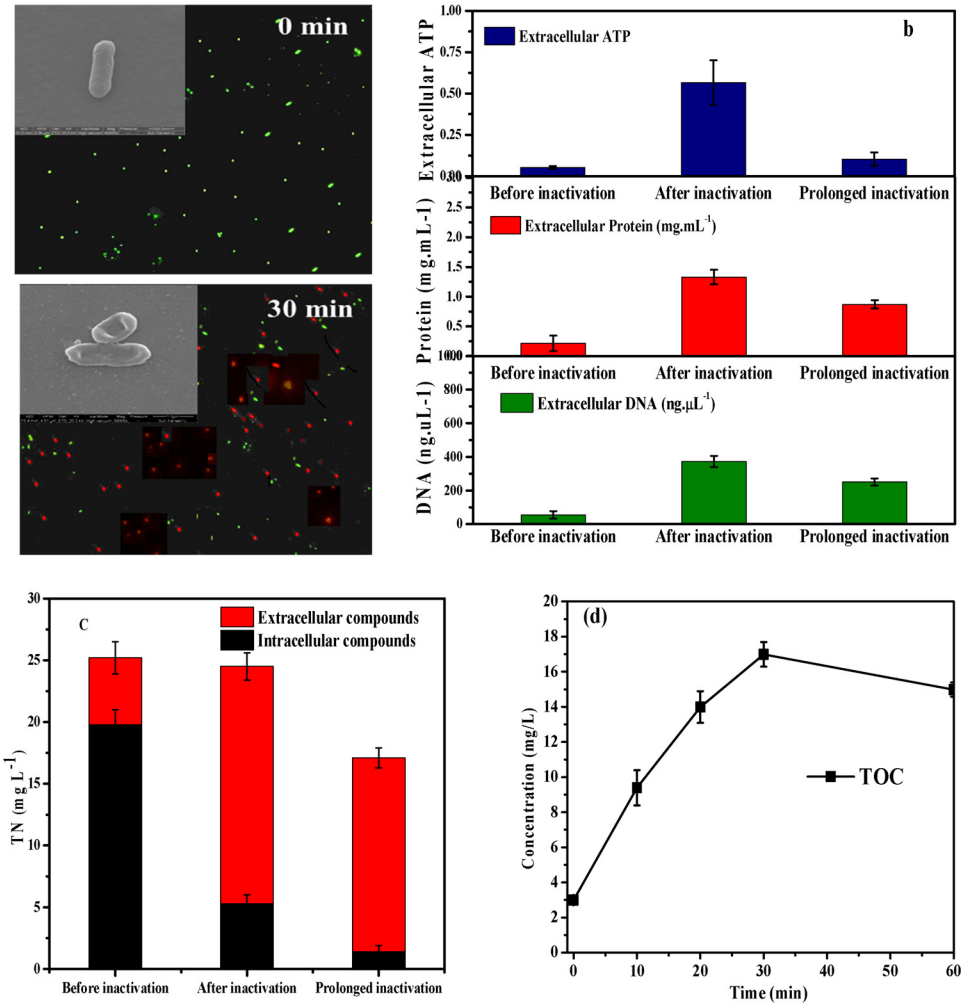

Fig. 5. Change of Extracellular ATP, protein, DNA, total nitrogen and Total organic carbon for *E. coli* before, after and prolonged inactivation. Reaction conditions: [*E. coli*] = 5 $\log_{10}$ cfu/mL, [ilmenite] = 1 g/L, [PS] = 0.5 mM.

chain oxidation reaction inner cell [62].

Accompanying with the destroyed cell membrane, the resultant ROS, can subsequently injure cells by reacting with various biomolecules. ATP is a key energy carrier, which are mainly survived on the cell membrane and can serve as an indicator of cell viability [40]. As shown in Fig. 5b, extracellular ATP concentration was limited before inactivation. By contrast, extracellular ATP increased significantly to 0.566 nmol after inactivation. The results confirm the permeability of *E. coli* cell membrane was changed after ROS attack and intracellular ATP was greatly released. Generally, ROS has been found to inhibit ATP formation either by behaving like a protonophore or by inhibiting enzymes in the respiratory chain to dissipate the proton motive force [63]. Due to the serious destruction of ATP synthesis chain in *E. coli*, the ATP value rapidly dropped to 0.103 nmol with prolonged reaction time.

Similarly, as shown in Fig. 5b, extracellular protein and DNA levels of *E. coli* increased after inactivation in the ilmenite/PS/Vis process. For instance, extracellular protein and DNA of *E. coli* increased to 373 mg/mL and 1.33 ng/μL respectively. The results indicated that ROS destroys the cell wall of *E. coli* and causes the release of intracellular organic compounds, thus leading to the inactivation of *E. coli* cells. With prolonged reaction time, the leaked protein and DNA further decreased to 250.1 mg/mL and 0.87 ng/μL, suggesting the degradation and even mineralization of leaked organic compounds by ROS. Notably, the decline rate of extracellular protein and DNA is much slower than that of ATP. Because ATP synthesis enzymes are mainly survived on the cell membrane, the present results may indicate the critical role of cell membrane, which is firstly attacked by ROS and then results in the leakage of intracellular components.

In general, protein and nucleic acids composed the main nitrogenous organic compounds in *E. coli* [64]. Fig. 5c shows the intracellular and extracellular changes of total nitrogen (TN) in *E. coli* before and after inactivation in the ilmenite/PS/Vis process. The results suggested that intracellular TN levels decreased, while extracellular TN levels increased significantly after inactivation. In other words, TN levels kept stable around 25 mg/L, but the intracellular TN was released and converted into extracellular TN. Furthermore, with the continued degradation and mineralization by ROS for long reaction, the content of leaked nitrogenous organic compounds quickly decreased from initial 25.2 to 17.1 mg/L. Moreover, as seen in Fig. 5d, the bulk TOC increased and reached a maximum at t = 30 min (16.8 mg C/L for TOC). Afterward, the TOC started to level off, suggesting that the bulk TOC could be further mineralized in the present system. In principle, the catalytic/photocatalytic oxidation end-products of carbon will be carbon dioxide (CO_2). Both decreases of TOC and TN contents indicate the present system can efficiently mineralize the inactivated cells.

As shown in Fig. 6, due to its strong oxidation capacity, ROS can destroy the cell wall and change the permeable pressure, thus leading to the changes in the shape of *E. coli* and leakage of intracellular compounds. The mechanism of *E. coli* inactivation in the ilmenite/PS/Vis system is similar to that of the inactivation of fungal spores, viruses, and

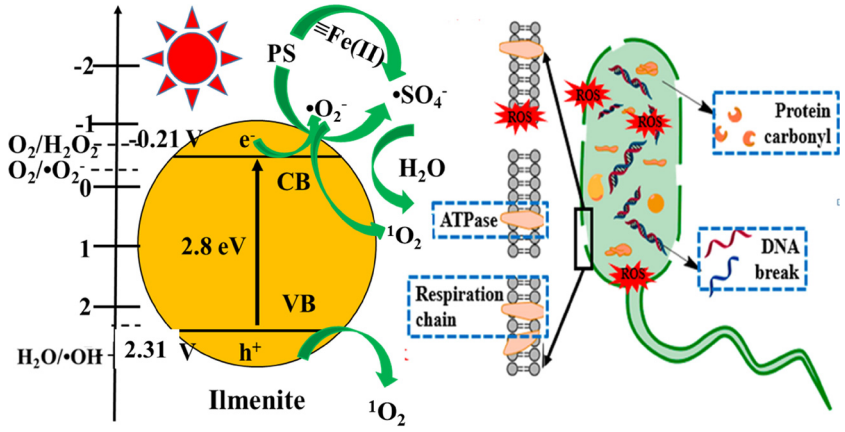

Fig. 6. Plausible mechanism of photocatalytic inactivation of *E. coli* in the ilmenite/PS/Vis process.

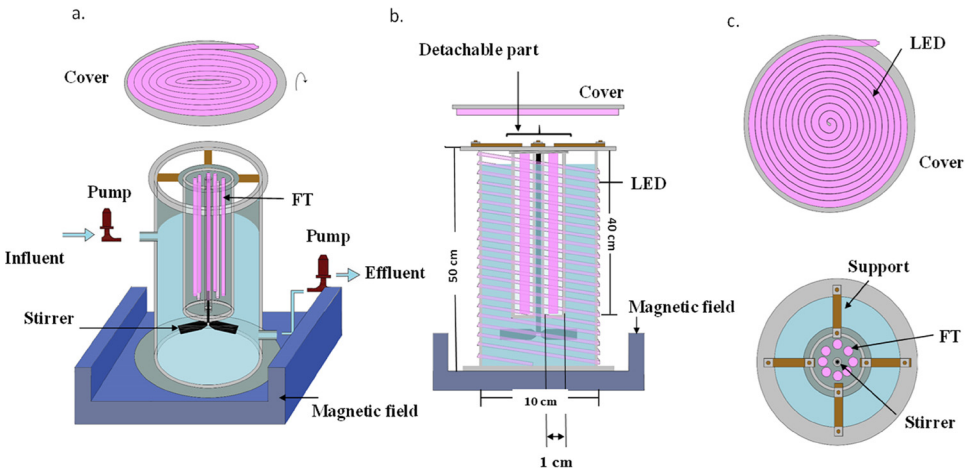

Fig. 7. (a) Pilot-scale photocatalytic disinfection reactor (25 L) with speed control, light control and electromagnetic force control devices for ilmenite, (b) the side-view, and (c) bottom-view of the reactor.

protozoa [38,65]. For instance, some researchers reported that ROS damages fungal spores' plasma membrane mainly by permeabilization, then induce the leakage of proteins, DNA, polysaccharides, potassium ions, and calcium ions [38].

3.6. Parameters optimization for bacterial inactivation in 25 L reactor

In order to provide a pilot-scale treatment device to settle the bacterial contamination in water, the inactivation experiment of *E. coli* was also conducted in the large volume (25 L) reactor (Fig. 7). A magnetic field was provided by turning on the circuit surrounding the device to hold the magnetic ilmenite, and the treated water sample can be drained from the bottom outlet(s). Then, the ilmenite can be reused in next run by adding new sample solution after turning off the magnetic field. The operational physical, chemical and biological parameters in the reactor were investigated to debug the reactor for treating wastewater. Moreover, the real wastewater collected from lake and domestic sectors were utilized to test its applicability.

3.6.1. Concentration of ilmenite

The bacterial inactivation efficiency using different concentration of ilmenite (0.1, 0.5, 1, 1.5 and 2 g/L) was investigated (Fig. 8a). The inactivation efficiency increases when the concentration of ilmenite increases from 0.1 to 1.5 g/L. Generally, with higher concentration of ilmenite, more reactive oxidative species (ROSs) can be produced and hence the inactivation efficiency increased. However, there is no significant difference between the 1, 1.5 and 2 g/L, indicating ilmenite concentrations higher than 1 g/L may inhibit the light irradiation and suspension dispersion, thus cannot further improve the bacterial inactivation. As ilmenite can be easily recollected and reused with a low cost, concentration of 1 g/L is thus suggested for the PS activation by ilmenite.

3.6.2. Concentration of PS

Fig. 8b presents the inactivation efficiencies of *E. coli* at a varying dosage of PS. The *E. coli* inactivation was enhanced with the PS concentration increased from 0.1 to 0.5 mM, respectively. This increased *E. coli* inactivation efficiency was mainly attributed to the accelerated photoelectrons' capture and enhanced radicals' generation that occurred with higher doses of PS. Further increasing the PS consistent with concentration to 1 mM did not enhance the inactivation efficiency but resulted in a slight inhibition, perhaps due to the quenching of $\cdot SO_4^-$ by ≡Fe(II) of ilmenite [26].

3.6.3. Effect of light intensity

Experiments to investigate the light intensity effect on photocatalytic disinfection efficiency of the ilmenite are performed using white LED lamp as light source. Light intensity range has been determined to guide turn on or off the LED lamp. Fig. 8c shows that the *E. coli* inactivation efficiency increased a little with the increasing of VL intensity from 0 to 6.4 mW/cm^2. Because more lights are provided, there are more photons for the ilmenite to produce ROSs for bacterial inactivation. In general, the higher of the light intensity, the better of the bacterial inactivation efficiency [16]. Meanwhile, in the light

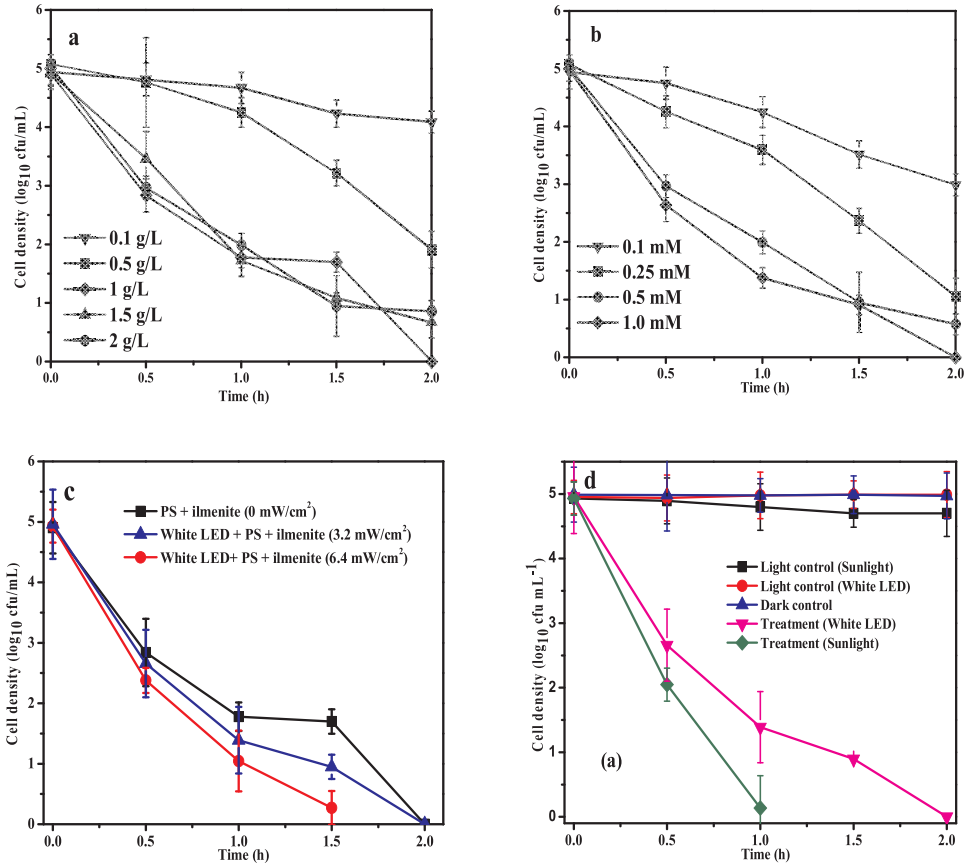

Fig. 8. Effect of (a) ilmenite amount, (b) PS concentration, (c) light intensity, (d) light source for bacterial inactivation in 25 L large-scale device. Experimental conditions: [*E. coli*] = 5 $\log_{10}$ cfu/mL, [ilmenite] = 0.1–2 g/L, [PS] = . 0.5–2 mM.

control with the light intensity of 6.4 mW/cm^2, the bacterial population remained constant after treatment, which suggests that the photolysis of VL is not effective to inactivate *E. coli*. Thus, the intensity of VL is also one of the most important parameters in the *E. coli* inactivation.

3.6.4. Effect of light sources

Light was proved to be an important role in PS activation. Besides artificial light emitting diode (LED) lamp, the light source was provided by authentic sunlight to save more energy (Fig. S3). As shown in Fig. 8d, total inactivation of 5 $\log_{10}$ cfu/mL of *E. coli* cells can be obtained within 1.5 h sunlight irradiation, while 2 h was needed for white LED lamp irradiation. The light intensity of sunlight has been measured (Fig. S4), mainly contains VL (20–42 mW/cm^2) and trace amount of UV (0–5 mW/cm^2) during experimental period. Since sunlight has VL with a higher intensity than white LED lamp and even traceable UV, more photons with higher energy would take part in the reaction and result in a higher inactivation performance [16]. Meanwhile, the reactor temperature under sunlight irradiation was determined to be in a range of 20–30 °C, which does not affect the bacterial inactivation efficiency, according to the observation of limited cells' loss in the light control.

3.6.5. Reusability and stability

Recycle and regeneration of catalyst is crucial for efficient application that will not only reduce cost but also eliminate secondary pollution. In order to study the stability of ilmenite, five consequent-runs experiment has been conducted by using the recycled ilmenite. In the first run, the *E. coli* (10^5 cfu/mL) in the system could be completely inactivated within 2 h under white LED lamp irradiation. However, the inactivation activities were decreased in the recycling experiment (Fig. 9a), which can be attributed to the accumulation of residual cell debris on the surface of ilmenite. Moreover, the oxidation of surface Fe (II) may cause passivation, this was also found in other treatment systems [66].

The iron leaching in the experiment has been monitored. In the system, the total Fe leaching increased to a level of 12.5 mg/L (Fig. 9b). It would be worthwhile observing that leached Fe (especially Fe^{2+}) might be problematic for some applications like wastewater treatment. Therefore, a further precipitation step may be needed to eliminate the dissolved Fe, which can be obtained by the addition of base like NaOH to form $Fe(OH)_3$. Moreover, the leached Fe^{3+} can be used as flocculants to help precipitate the ions or suspended solid (SS) in the water [67].

Moreover, concerning the XPS of the Fe 2p spectrum after use (Fig. 9c, d), the presence of a band at 710 eV and another at 724 eV corresponds to Fe(II), while the bands centered at 712 eV and 725 eV corresponds to Fe(III). The fitting peaks of ilmenite before use indicated the surface amounts of 43.76/56.23 for Fe(II)/Fe(III). However, in the case of the ilmenite after use the surface amounts were 40.18/59.82 for Fe(II)/Fe(III). The increased Fe(III) peak can be ascribed to the presence of iron sulfate generated on the ilmenite surface. For instance, Al-Shamsiand et al. detected $FeSO_4$ at a binding energy of 711.1 eV in the Fe 2p spectra of used nZVI [68]. Descostes et al. also revealed that iron oxides ($FeSO_4$, $Fe_2(SO_4)_3$, Fe_2O_3) were formed on pyrite at 711.55 eV [69]. Therefore, the surface oxidation of ilmenite results in the partially loss of its activity.

3.6.6. Effect of authentic water matrix

In order to provide a pilot-scale reactor to settle the bacterial contamination in the wastewater, the authentic wastewater collected from domestic and industrial sectors were utilized to test the bacterial inactivation. As shown in Fig. 10a, there was great inhibition in the *E. coli* inactivation of the sewage effluent (3 $\log_{10}$ cfu/mL of residual cells) and surface water (1.2 $\log_{10}$ cfu/mL of residual cells) for 3 h treatment. The

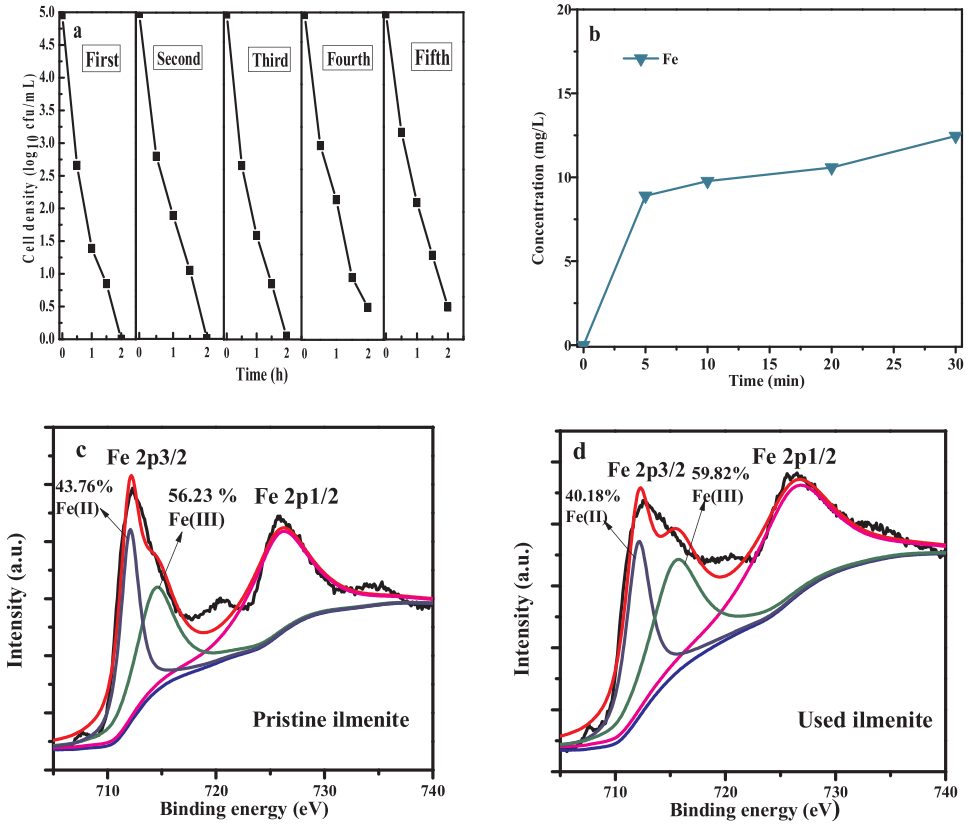

Fig. 9. (a) Reusability of ilmenite, (b) Leakage of Fe ions in ilmenite/PS system; XPS of Fe spectra in pristine (c) and reused ilmenite (d). Experimental conditions: [*E. coli*] = 5 $\log_{10}$ cfu/mL, [ilmenite] = 1 g/L, [PS] = 0.5 mM.

inhibition was mainly caused by the natural water components like natural organic matter (TOC represents NOM) and inorganic ions (bicarbonate, etc.). According to Table S2, the chemical oxygen demand (COD) of the treatment sewage effluent was 28 mg O_2/L, and the sample collected from Weiyuan Lake of The Chinese University of Hong Kong was determined to be 11.6 mg O_2/L. As mentioned, organic matter will stick on the surface of ilmenite and consume the ROSs. Moreover, ROS like $\cdot O_2^-$ can react selectively against the prevailed nitrogen-containing organics in NOM, while $\cdot SO_4^-$ may complex or react with CO_3^{2-}, also can greatly inhibit bacterial inactivation [70]. The results suggest that ilmenite screened in this project is active enough to deal with wastewater with very high organic loading. This is because the $^1O_2$-mediated oxidative system possesses a high selectivity, which can suffer less interference from common background organic and inorganic substances in water, evidenced by Shao et al. [71]. Even though, more parameters like temperature and pH, etc. should be investigated to satisfy the requirement of real application.

In order to completely eliminate the bacterial cells and debris in the solution or on the surface of catalyst, Jacoby et al. firstly reported the complete degradation (mineralization) of organic compounds in the bacterial cells into CO_2 by catalysis [72]. Therefore, total organic carbon (TOC) of the treated samples has been measured to quantitatively investigate the level of mineralization in the present system [73]. During the inactivation process, it is observed an approximately 16% reduction of the TOC in SW and 3% reduction in WW within 3 h of reaction time (Fig. 10b). It is interesting to note that, although the *E. coli* in both water matrix has been partially inactivated, but the TOC decrease is not significant. These results suggest that the presence of TOC negatively influenced *E. coli* inactivation, perhaps due to the $^1O_2$-mediated oxidative system possess a high selectivity towards organic *E. coli* [71]. The TOC removal still needs a prolonged irradiation time to obtain a total mineralization.

4. Conclusion

A natural magnetic mineral, namely ilmenite, was screened and employed for *E. coli* inactivation under visible light irradiation. Ilmenite could inactivate *E. coli* via the limited $\cdot O_2^-$ under VL irradiation but with an unsatisfactory inactivation efficiency. The introduction of PS significantly accelerated the *E. coli* inactivation of in the ilmenite/PS/Vis process. The results of PL spectra and electrochemical measurements together with EPR analysis revealed that the introduced PS could suppress the recombination of photo-generated electrons and holes, as well as the ≡Fe(II) of ilmenite facilitate PS activation, thus increasing the production of reactive radicals like $^1O_2$, $\cdot O_2^-$, $\cdot SO_4^-$, thereby accelerating the inactivation of *E. coli*. Moreover, the ilmenite showed good inactivation performance in authentic water matrix and maintained good reusability in the pilot-scale 25 L reactor. It is anticipated that this study could provide a new persulfate-mediated photocatalytic process for microbial control and widen the application range of natural mineral as photocatalysts and catalysts.

Acknowledgements

The project was supported by a research grant (GRF14100115) of the Research Grant Council, Hong Kong SAR Government and the Technology and Business Development Fund (TBF15SCI008) of The Chinese University of Hong Kong to P.K. Wong, and the research grants (51578556, 21673086, and 41603097) of National Science Foundation of China to C. He and D.H. Xia, respectively. P.K. Wong was also supported by CAS/SAFEA International Partnership Program for Creative Research Teams of Chinese Academy of Sciences (2015HSC-UE004). Dr. Xia was also supported by the Start-up Funds for High-Level Talents of Sun Yat-sen University (38000-18821111).

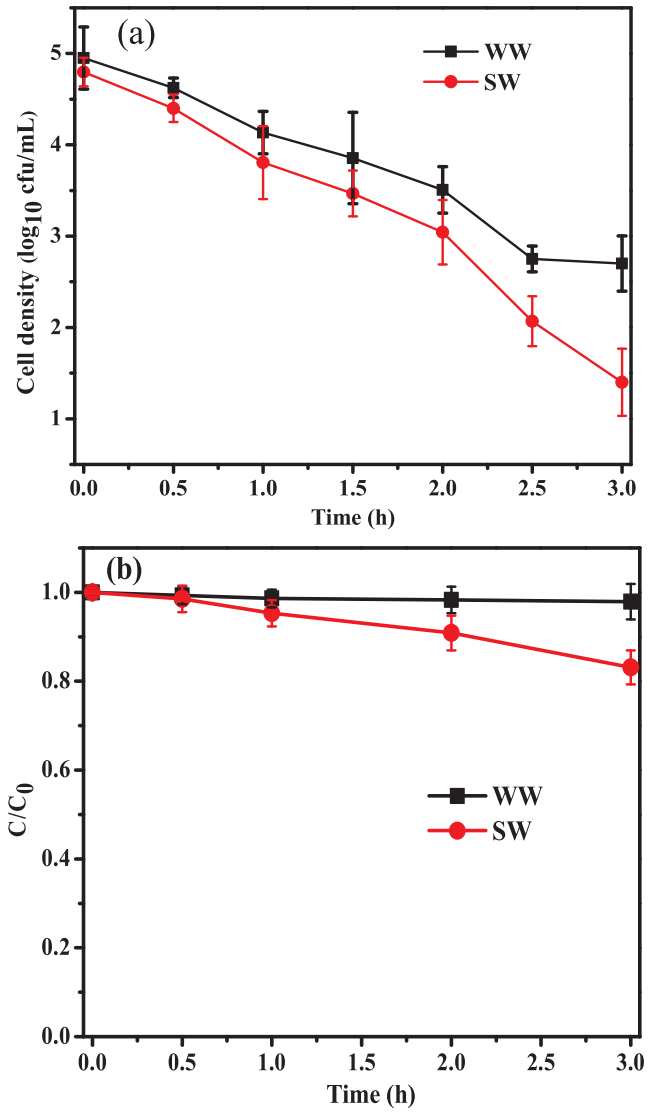

Fig. 10. (a) Bacterial inactivation in 25 L large-scale device with different water matrix by ilmenite (secondary wastewater effluent = WW, surface water = SW); (b) The amount of TOC during treatment. Experimental conditions: [*E. coli*] = 5 $\log_{10}$ cfu/mL, [ilmenite] = 1 g/L, [PS] = 0.5 mM.

Appendix A. Supplementary data

Supplementary material related to this article can be found, in the online version, at doi:https://doi.org/10.1016/j.apcatb.2018.07.003.

References

[1] N.F.F. Moreira, C. Narciso-da-Rocha, M.I. Polo-López, L.M. Pastrana-Martínez, J.L. Faria, C.M. Manaia, P. Fernández-Ibáñez, O.C. Nunes, A.M.T. Silva, Water Res. 135 (2018) 195–206.
[2] E.M. Anastasi, T.D. Wohlsen, H.M. Stratton, M. Katouli, Water Res. 47 (2013) 6670–6679.
[3] S. Loeb, C. Li, J.-H. Kim, Environ. Sci. Technol. 52 (2017) 205–213.
[4] D. Xia, Y. Li, G. Huang, C.C. Fong, T. An, G. Li, H.Y. Yip, H. Zhao, A. Lu, P.K. Wong, Appl. Catal. B Environ. 176–177 (2015) 749–756.
[5] D. Xia, W. Wang, R. Yin, Z. Jiang, T. An, G. Li, H. Zhao, P.K. Wong, Appl. Catal. B: Environ. 214 (2017) 23–33.
[6] Q. Yin, L. Tan, Q. Lang, X. Ke, L. Bai, K. Guo, R. Qiao, S. Bai, Appl. Catal. B: Environ. 224 (2018) 671–680.
[7] D. Xia, Z. Shen, G. Huang, W. Wang, J. Yu, P.K. Wong, Environ. Sci. Technol. 49 (2015) 6264–6273.
[8] N.F.F. Moreira, C. Narciso-da-Rocha, M.I. Polo-Lopez, L.M. Pastrana-Martínez, J.L. Faria, M. Munoz, P. Domínguez, Z.M. de Pedro, J.A. Casas, J.J. Rodriguez, Appl. Catal. B: Environ. 203 (2017) 166–173.
[9] J. Rodríguez-Chueca, M.I. Polo-Lopez, R. Mosteo, M.P. Ormad, P. FernandezIbanez, Appl. Catal. B: Environ. 150–151 (2014) 619–629.
[10] D. Xia, T.W. Ng, T. An, G. Li, Y. Li, H.Y. Yip, H. Zhao, A. Lu, P.K. Wong, Environ. Sci. Technol. 47 (2013) 11166–11173.
[11] D. Xia, R. Yin, J. Sun, T. An, G. Li, W. Wang, H. Zhao, P.K. Wong, J. Hazard. Mater. 340 (2017) 435–444.
[12] D. Xia, H. Liu, Z. Jiang, T.W. Ng, W.S. Lai, T. An, W. Wang, P.K. Wong, Appl. Catal. B: Environ. 224 (2018) 541–552.
[13] A. Lu, Y. Li, M. Lv, C. Wang, L. Yang, J. Liu, Y. Wang, K.H. Wong, P.K. Wong, Sol. Energy Mater. Sol. Cells 91 (2007) 1849–1855.
[14] Y. Li, Y. Li, Y. Yin, D. Xia, H. Ding, C. Ding, J. Wu, Y. Yan, Y. Liu, N. Chen, P.K. Wong, A. Lu, Appl. Catal. B: Environ. 226 (2018) 324–336.
[15] Y. Chen, A. Lu, Y. Li, L. Zhang, H.Y. Yip, H. Zhao, T. An, P.K. Wong, Environ. Sci. Technol. 45 (2011) 5689–5695.
[16] Y. Chen, T.W. Ng, A. Lu, Y. Li, H.Y. Yip, T. An, G. Li, H. Zhao, M. Gao, P.K. Wong, Chem. Eng. J. 234 (2013) 43–48.
[17] X. Yang, Y. Li, A. Lu, Y. Yan, C. Wang, P.K. Wong, Sol. Energy Mater. Sol. Cells 95 (2011) 1915–1921.
[18] P. Avetta, A. Pensato, M. Minella, M. Malandrino, V. Maurino, C. Minero, K. Hanna, D. Vione, Environ. Sci. Technol. 49 (2015) 1043–1050.
[19] P. García-Muñoz, G. Pliego, J.A. Zazo, B. Barbero, A. Bahamonde, J.A. Casas, Chem. Eng. J. 318 (2017) 89–94.
[20] L. Luo, D. Wu, D. Dai, Z. Yang, L. Chen, Q. Liu, J. He, Y. Yao, Appl. Catal. B: Environ. 205 (2017) 404–411.
[21] J.E. Silveira, W.S. Paz, P. Garcia-Munoz, J.A. Zazo, J.A. Casas, Appl. Catal. B: Environ. 219 (2017) 314–321.
[22] Y. Gao, Z. Zhang, S. Li, J. Liu, L. Yao, Y. Li, H. Zhang, Appl. Catal. B: Environ. 185 (2016) 22–30.
[23] S. Ahn, T.D. Peterson, J. Righter, D.M. Miles, P.G. Tratnyek, Environ. Sci. Technol. 47 (2013) 11717–11725.
[24] I. Michael-Kordatou, M. Iacovou, Z. Frontistis, E. Hapeshi, D.D. Dionysiou, D. Fatta-Kassinos, Water Res. 85 (2015) 346–358.
[25] A.R. Chesney, C.J. Booth, C.B. Lietz, L. Li, J.A. Pedersen, Environ. Sci. Technol. 50 (2016) 7095–7105.
[26] D. Xia, Y. Li, G. Huang, R. Yin, T. An, G. Li, H. Zhao, A. Lu, P.K. Wong, Water Res. 112 (2017) 236–247.
[27] M. Kamagate, A.A. Assadi, T. Kone, L. Coulibaly, K. Hanna, J. Hazard. Mater. 346 (2018) 159–166.
[28] Y. Gao, S. Li, Y. Li, L. Yao, H. Zhang, Appl. Catal. B: Environ. 202 (2017) 165–174.
[29] Y. Wang, X. Zhao, D. Cao, Y. Wang, Y. Zhu, Appl. Catal. B: Environ. 211 (2017) 79–88.
[30] A.D. Bokare, W. Choi, Environ. Sci. Technol. 49 (2015) 14392–14400.
[31] X. Cheng, H. Guo, Y. Zhang, X. Wu, Y. Liu, Water Res. 113 (2017) 80–88.
[32] M.A. Al-Shamsi, N.R. Thomson, Ind. Eng. Chem. Res. 52 (2013) 13564–13571.
[33] H. Kim, W. Kim, Y. Mackeyev, G.S. Lee, H.J. Kim, T. Tachikawa, S. Hong, S. Lee, J. Kim, L.J. Wilson, T. Majima, P.J.J. Alvarez, W. Choi, J. Lee, Environ. Sci. Technol. 46 (2012) 9606–9613.
[34] J.A. Zazo, G. Pliego, P. García-Mu˜noz, J.A. Casas, J.J. Rodriguez, Appl. Catal. B: Environ. 192 (2016) 350–356.
[35] M. Munoz, P. Dominguez, Z.M. de Pedro, J.A. Casas, J.J. Rodriguez, Appl. Catal. B: Environ. 203 (2017) 166–173.
[36] M.R. Eskandarian, M. Fazli, M.H. Rasoulifard, H. Choi, Appl. Catal. B: Environ. 4 (2016) 407–416.
[37] O. Tokode, R. Prabhu, L.A. Lawton, P.K.J. Robertson, Chem. Eng. J. 246 (2014) 337–342.
[38] G. Wen, X. Xu, T. Huang, H. Zhu, J. Ma, Water Res. 125 (2017) 132–140.
[39] P. Desjardins, J.B. Hansen, M. Allen, Microvolume spectrophotometric and fluorometric determination of protein concentration. Current Prot. Protein Sci., Chapter 3 (2009) 3. 10.1-3.10.16.
[40] F. Hammes, F. Goldschmidt, M. Vital, Y. Wang, T. Egli, Water Res. 44 (2010) 3915–3923.
[41] A.L. Teel, M. Ahmad, R.J. Watts, J. Hazard. Mater. 196 (2011) 153–159.
[42] T. Yamashita, P. Hayes, Appl. Surf. Sci. 254 (2008) 2441–2449.
[43] X. Duan, H. Sun, J. Kang, Y. Wang, S. Indrawirawan, S. Wang, ACS Catal. 5 (2015) 4629–4636.
[44] Y. Guan, J. Ma, Y. Ren, Y. Liu, J. Xiao, L. Lin, C. Zhang, Water Res. 47 (2013) 5431–5438.
[45] Y. Wang, X. Zhao, D. Cao, Y. Wang, Y. Zhu, Appl. Catal. B: Environ. 211 (2017) 79–88.
[46] G. Liu, S. You, Y. Tan, N. Ren, Environ. Sci. Technol. 51 (2017) 2339–2346.
[47] Y. Zhou, J. Jiang, Y. Gao, J. Ma, S.Y. Pang, J. Li, X.T. Lu, L.P. Yuan, Environ. Sci. Technol. 49 (2015) 12941–12950.
[48] G.-D. Fang, D.D. Dionysiou, Souhail R. Al-Abed, D.-M. Zhou, Appl. Catal. B: Environ. 98 (2013) 27–38.
[49] C. Tan, N. Gao, Y. Deng, J. Deng, S. Zhou, J. Li, X. Xin, J. Hazard. Mater. 276 (2014) 452–460.
[50] X.L. Qu, P.J.J. Alvarez, Q.L. Li, Environ. Sci. Technol. 47 (2013) 14080–14088.
[51] C.Y. Chen, C.T. Jafvert, Environ. Sci. Technol. 44 (2010) 6674–6679.
[52] Y. Lei, C.-S. Chen, Y.-J. Tu, Y.-H. Huang, H. Zhang, Environ. Sci. Technol. 49 (2015) 6838–6845.
[53] O.S. Furman, A.L. Teel, R.J. Watts, Environ. Sci. Technol. 44 (2010) 6423–6428.
[54] H. Lee, H. Kim, S. Weon, W. Choi, Y.S. Hwang, J. Seo, C. Lee, J.-H. Kim, Environ. Sci. Technol. 50 (2016) 10134–10142.
[55] X. Li, J.Y. Liu, A.I. Rykov, H. Han, C. Jin, X. Liu, J.H. Wang, Appl. Catal. B: Environ. 179 (2015) 196–205.
[56] Y. Zhang, H.P. Tran, X. Du, I. Hussain, S. Huang, S. Zhou, W. Wen, Chem. Eng. J. 308 (2017) 1112–1119.

[57] J. Huang, Q. Shang, Y. Huang, F. Tang, Q. Zhang, Q. Liu, S. Jiang, F. Hu, W. Liu, Y. Luo, T. Yao, Y. Jiang, Z. Pan, Z. Sun, S. Wei, Angew. Chem. Int. Ed. 54 (2015) 1–6.
[58] D. Xia, T. An, G. Li, Y. Li, H.Y. Yip, H. Zhao, P.K. Wong, Water Res. 99 (2016) 149–161.
[59] Y. Huang, W. Fan, B. Long, H. Li, F. Zhao, Z. Liu, Y. Tong, H. Ji, Appl. Cata. B: Environ. 185 (2016) 68–76.
[60] Y. Nosaka, A.Y. Nosaka, Chem. Rev. 117 (2017) 11302–11336.
[61] Y. Yang, J. Wen, J. Wei, R. Xiong, J. Shi, C. Pan, ACS Appl. Mater. Interfaces. 5 (2013) 6201–6207.
[62] H. Sun, G. Li, X. Nie, H. Shi, P.K. Wong, H. Zhao, T. An, Environ. Sci. Technol. 48 (2014) 9412–9419.
[63] K.M. Parker, T. Zeng, J. Harkness, A. Vengosh, W.A. Mitch, Environ. Sci. Technol. 48 (2014) 11161–11169.
[64] O.K. Dalrymple, E. Stefanakos, M.A. Trotz, D.Y. Goswami, Appl. Catal. B: Environ. 98 (2010) 27–38.
[65] M.T. Madigan, J.M. Martinko, J. Parker, Brock Biology of Microorganisms, 13 ed, Prentice Hall, New Jersey, 2012.
[66] A. Gamalski, J. Tersoff, S. Kodambaka, D. Zakharov, F. Ross, E. Stach, Nano Lett. 15 (2015) 8211–8216.
[67] J. Xin, F. Tang, X. Zheng, H. Shao, O. Kolditz, X. Lu, Water Res. 100 (2016) 80–87.
[68] M.A. Al-Shamsi, N.R. Thomson, Ind. Eng. Chem. Res. 52 (2013) 13564–13571.
[69] M. Descostes, F. Mercier, N. Thromat, C. Beaucaire, M. Gautier-Soyer, Appl. Surf. Sci. 165 (2000) 288–302.
[70] C. Michael-Kordatou, X. Michael, X. Duan, D. He, M.A. Dionysiou, Fatta-Kassinos, D. Mills, Water Res. 77 (2015) 213–248.
[71] P. Shao, J. Tian, F. Yang, X. Duan, S. Gao, W. Shi, X. Luo, F. Cui, S. Luo, S. Wang, Adv. Funct. Mater. 28 (2018) 1705295.
[72] W.A. Jacoby, P.C. Maness, E.J. Wolfrum, D.M. Blake, J.A. Fennell, Environ. Sci. Technol. 32 (1998) 2650–2653.
[73] C.M. Manaia, P. Fernandez-Ibanez, O.C. Nunes, A.M.T. Silva, Water Res. 135 (2018) 195–206.